Arabian Journal of Chemistry (2019) **12**, 1454–1462

King Saud University

Arabian Journal of Chemistry

www.ksu.edu.sa
www.sciencedirect.com

ORIGINAL ARTICLE

TiO_2/clay as a heterogeneous catalyst in photocatalytic/photochemical oxidation of anionic reactive blue 19

Haithem Bel Hadjltaief [a], Maria Elena Galvez [b,c], Mourad Ben Zina [a], Patrick Da Costa [b,c,*]

[a] *Laboratoire Eau, Energie et Environnement (LR3E), Code: AD-10-02, Ecole Nationale d'Ingénieurs de Sfax, Université de Sfax, B.P1173.W.3038, Sfax, Tunis, Tunisia*
[b] *Univ. Paris 6, UPMC Sorbonne Universités, Institut Jean Le Rond d'Alembert, 2 place de la gare de ceinture, 78210 Saint Cyr L'Ecole, France*
[c] *Institut Jean Le Rond d'Alembert, UMR CNRS 7190, 2 place de la gare de ceinture, 78210 Saint Cyr L'Ecole, France*

Received 22 August 2014; accepted 3 November 2014
Available online 10 November 2014

KEYWORDS

Anionic reactive blue 19;
TiO_2-coated Tunisian clay;
Photocatalytic degradation;
UVA and solar irradiation

Abstract A TiO_2-coated Tunisian clay (TiO_2–clay) was synthesized by a typical impregnation method. The physicochemical characterization points to a successful impregnation of titania on the clay surface. The activity of this structured catalyst was studied in the photocatalytic/photochemical oxidation of anionic reactive blue 19 (RB 19). The effect of UVA and solar irradiation (UV-solar) was studied at room temperature. TiO_2–clay demonstrated an effective degradation of RB 19 under both types of irradiation. Moreover, in this study, the effects of various oxidants such as hydrogen peroxide (H_2O_2), potassium peroxodisulfate ($K_2S_2O_8$) and sodium carbonate (Na_2CO_3) were thoroughly investigated. H_2O_2 was a promising oxidant for promoting RB 19 degradation under UV_A. The kinetics of discoloration of RB 19 followed a pseudo-first-order rate law. We can remark that 20 min of UV irradiation was enough to achieve 100% discoloration of the aqueous solution. However, under UV–Vis, HPLC and chemical oxygen demand measurements indicated, that a longer reaction time (of around 45 min) was required for achieving the complete dye mineralization. The findings clearly demonstrated the applicability of this TiO_2/clay catalyst for the photocatalytic oxidation of RB 19.
© 2014 The Authors. Production and hosting by Elsevier B.V. on behalf of King Saud University. This is an open access article under the CC BY-NC-ND license (http://creativecommons.org/licenses/by-nc-nd/3.0/).

* Corresponding author at: Institut Jean Le Rond d'Alembert, UMR CNRS 7190, 2 place de la gare de ceinture, 78210 Saint Cyr L'Ecole, France. Tel.: +33 1 30 85 48 65; fax: +33 1 30 85 48 99.
E-mail address: patrick.da_costa@upmc.fr (P. Da Costa).
Peer review under responsibility of King Saud University.

ELSEVIER Production and hosting by Elsevier

1. Introduction

Dyes are widely used in broad industrial sectors such as textile manufacturing, leather tanning, cosmetics, paper, food processing, and pharmaceutical industries. Various classes of dyes exist such as azo, anthraquinone, reactive, acidic, basic, neutral, disperse and direct dyes. Azo and anthraquinone dyes

http://dx.doi.org/10.1016/j.arabjc.2014.11.006
1878-5352 © 2014 The Authors. Production and hosting by Elsevier B.V. on behalf of King Saud University.
This is an open access article under the CC BY-NC-ND license (http://creativecommons.org/licenses/by-nc-nd/3.0/).

are however the most commonly used (Carneiro et al., 2007; McCallum et al., 2000). These later ones constitute more than 60% of reactive dyes.

Among them, reactive blue 19 (RB 19) is easily available and commonly used in the textile industries (Guimarães et al., 2012). Researchers are concerned about mutagenic properties of RB 19 due to the presence of electrophilic Vinyl Sulfone groups (Guimarães et al., 2012; Siddique et al., 2011). A wide range of methods have been developed for the removal of RB19 dye from the wastewaters such as biological methods (Wang et al., 2009), membrane filtration (Koyuncu, 2002), coagulation–flocculation (Jiang et al., 2011), electrocoagulation (Pirkarami et al., 2013; Song et al., 2008), adsorption (Gok et al., 2010; Moussavi and Mahmoudi, 2009) and advanced oxidation (AOPs) processes (He et al., 2008; Guimarães et al., 2012; De Souza et al., 2008). Among these techniques, photocatalysis constitutes one of the emerging technologies for the degradation of organic pollutants (Guimarães et al., 2012; Qu et al., 2013). Several advantages of this process over competing processes are: (1) complete mineralization, (2) no waste-solid disposal problem, and (3) only mild temperature and pressure conditions are necessary.

Clays possess certain properties which make them an ultimate choice as adsorbents or catalysis support such as low cost, high mechanical and chemical stability, availability, affordability, ion exchange capability, and environmentally friendly material (Garrido-Ramírez et al., 2010; Herney-Ramirez et al., 2010). Generally, whatever the particular application, the degradation or adsorption efficiency reached strongly depends on the catalyst origin and features, as well as on the operational conditions employed. As a result, it turns out to be necessary to evaluate the influence of these parameters on the efficiency of each particular catalytic system, in order to determine the viability of its practical use. For example, the use of Tunisian clays has not been explored very much. Promising results have been obtained in the degradation or adsorption of model pollutants such as volatile organic compound (Dammak et al., 2013), phenol (Bel Hadjltaief et al., 2014), heavy metals (Eloussaief and Mourad, 2010), dyes and more complex organic compounds such as the malachite green and red Congo (Bel Hadjltaief et al., 2013), and also used in the purification of industrial phosphoric acid (Hamza et al., 2013). TiO_2-based clays (Dvininova et al., 2009; Djellabi et al., 2014. Chen et al., 2014) have attracted growing interest because of their low toxicity, such kind of materials is being used as photocatalysts for efficient treatment of wastewaters containing toxic organic compounds. Several preparation methods for TiO_2 supported on natural clay, such as hydrothermal, sol–gel, boil deposition, dip coating, metal organic chemical vapor deposition (MOCVD), and impregnation have been reported. To the best of our knowledge, the use of TiO_2 located on Tunisian clay, in the present context is very limited. For this reason, we have used TiO_2 located on Tunisian clay as catalysis for the photodecomposition of reactive blue.

The aim of this study was to determine the effectiveness of the photocatalytic and photo-chemical performance of processes based on UV and visible irradiations in the presence of TiO_2-coated Tunisian clay to remove anionic reactive blue from aqueous solution, determining the feasibility for the practical use of this catalytic process. Moreover, the photochemical activity of TiO_2−Clay was further investigated in the presence of several oxidants such as hydrogen peroxide (H_2O_2), potassium peroxodisulfate ($K_2S_2O_8$) and sodium carbonate (Na_2CO_3) under UVA irradiations. In addition, a kinetic study of the degradation of RB19 has been performed. Finally, the mineralization/degradation of the process was monitored by UV–Vis absorption spectra to investigate the structural change of R19, HPLC and DCO.

2. Experimental

2.1. Materials and chemicals

The clay used in this study was sampled in Jebel Tejera-Esghira deposits located in the Southeast of Tunisia from the area of Medenine. The natural clay was first purified by dispersion in water, decantation and extraction of the fraction with a particle size smaller than 2 μm. Then, the natural clay was modified by a sodium exchange described in our previous work (Bel Hadjltaief et al., 2014).

Titanium(IV)-isopropoxide, ($Ti(OPr^i)_4$, TTIP, 97%) purchased from Aldrich and obtained from Degussa Chemical was used as titanium source for the preparation of TiO_2−Clay photocatalyst. Anionic reactive blue 19 (RB19) was purchased from Aldrich chemical company. Hydrogen peroxide (H_2O_2(35%)), potassium peroxodisulfate ($K_2S_2O_8$ (99%)), sodium carbonate (97%), acetonitrile, sodium hydroxide, hydrochloric acid and phosphoric acid, high-purity analytical grade reagents were supplied by Sigma–Aldrich.

The TiO_2−clay photocatalyst was prepared by a typical impregnation method. First, a fixed amount (5.0 g) of Na^+−clay (particle size < 63 μm) was added under stirring into the 20 mL of TTIP solution. The temperature of the mixing has been fixed at 150 °C in order to activate the reaction of titanium deposition during 5 h. After the impregnation process, the samples were washed with Milli-Q water to remove any free TiO_2 particles that were not physisorbed or chemisorbed to the Na^+−clay support. The TiO_2−clay samples have been filtered, and dried at 125 °C for 24 h. Finally, the dried material was calcined to 500 °C for 3 h in a nitrogen-purged reactor tube with a heating rate of 5 °C/min.

2.2. Raw clay and photocatalyst physico-chemical characterization

Several techniques were employed for the characterization of the samples. In order to determine the crystal phase composition and the crystallite size of the photocatalysts, X-ray diffraction measurements were carried out at room temperature using a X-ray diffractometer and Philips® PW 1710 diffractometer (Cu Kα, 40 kV/40 mA, scanning rate of 2θ per min). The crystallite size was calculated by X-ray line-broadening analysis using Scherrer equation. S_{BET} surface areas of the solids were measured by nitrogen adsorption at −196 °C using a Micrometitics ASAP 2010 analyzer. The samples with particles of a size lower than 100 m were firstly degassed at 60 °C for 72 h. The surface functional groups were studied by using

Fourier transform infrared (FT-IR) spectroscopy (IR, Digilab Excalibur FTS 3000 spectrometer). The morphology of the samples was studied using scanning electronic microscopy (SEM, Hitachi SU-70). Thermal analysis measurements were performed using a Set Soft 2000 apparatus. The dried samples were treated under nitrogen; the temperature was raised at a rate of 100 °C min^{-1} from room temperature to 900 °C.

2.3. Photo-catalytic reactor and activity tests

Photocatalytic performances of TiO_2–Clay catalysts were evaluated in the photodegradation of anionic reactive blue 19 (RB19) under either artificial solar light or UV-lamp (UV-A (365 nm), Black-Ray B 100 W UV-lamp, V-100AP series). In a typical process, aqueous solution of RB19 (75 mg/L, 200 mL) and photocatalysts (100 mg) were put into a 250 mL Pyrex reactor equipped with a magnetic stirrer (150 rpm) at a room temperature of 25 °C. In all runs, the distance between the aqueous dye solution and the UV source was kept constant at 15 cm. The reaction solution was firstly stirred for 30 min in the dark to achieve adsorption equilibrium. The photocatalytic reaction was then started by solar light or UVA-lamp. In a photochemical reaction, oxidants 8 mL of the H_2O_2, $K_2S_2O_8$ or Na_2CO_3 (prepared from 250 mg/L of H_2O_2 (35%), $K_2S_2O_8$ (98%) or Na_2CO_3 (98%)) were added into the reaction solution just before switching on the light.

2.4. Analytical methods

The disappearance of RB19 was analyzed either by UV–Vis spectrophotometer chemical oxygen demand (COD) or by HPLC. UV–vis spectrophotometer from Shimadzu was used to analyze the concentration of Rb19 dye solution as the reaction proceeds. The analysis was carried out with a 5 mL glass cuvette (1 cm square path length) and measured at the established maximum absorbance wavelength (λ_{max} = 591 nm) which was determined from absorption spectra. Chemical oxygen demand (COD) was determined using the reactor digestion method based on the method of acidic oxidation by bichromate (Emna et al., 2009).

The extent of discoloration efficiency and mineralization efficiency is measured according to Eqs. (1) and (2), respectively.

$$\text{Discoloration efficiency } \eta\ (\%) = (C_0 - C_t)/C_0 \times 100 \quad (1)$$

$$\text{Mineralization efficiency } \eta\ (\%) = (\text{COD}_0 - \text{COD}_t)/\text{COD}_0 \times 100 \quad (2)$$

where C_0 and COD_0 are the initial concentration and COD of the dyes and C_t and COD_t are the concentration and COD of the dyes at the specific reaction time (min), respectively.

The objectif of HPLC detection is to determinate the full degradation intermediaries of Rb19. The quantitative analyses of RB19 and its oxidation products were made by high liquid chromatography using a Perkin Elmer 200 series HPLC apparatus. The products formed are separated on a C_{18} column and then analyzed quantitatively using a UV-V detector measuring the optical density at 592 nm during 15 min. The mobile phase was a mixture of 70% acetonitrile and 30% sulfuric acid (5×10^{-2} mol L^{-1}). The mobile flow rate was fixed at 0.5 mL min^{-1}.

3. Results and discussion

3.1. Raw clay and catalyst characterization

Fig. 1 shows the nitrogen adsorption–desorption isotherms of the raw and modified clay samples. The adsorption isotherm of raw clay is type III (BDDT classification (Sing et al., 1985)), which is characteristic of nitrogen adsorption on macroporous adsorbents whereas the adsorption isotherms of the TiO_2–clay sample is type IV, corresponding to mesoporous adsorbents. This suggests that most of the total porosity consists of mesoporosity. The hysteresis loops of these isotherms seem to be of type H3 (IUPAC classification (Sing and Williams, 2004)), corresponding to slit-shaped pores in layered materials. As shown in Table 1, the specific surface area (S_{BET}) increases from 36.6 to 116.7 m^2/g and the total pore volume was increased from 0.13 to 0.26 cm^3/g. This large increase in the surface area and the total pore volume of TiO_2–Clay indicates the successful pillaring of the TiO_2 species into the silicate layers of the clay.

The X-ray diffraction (XRD) patterns of raw and modified clay material catalyst are shown in Fig. 2. The crystalline structure of the raw clay identified by XRD measurements (Fig. 2) showed that clay is composed mainly of quartz (26.7°), kaolinite (22.8°) and illite (12.6°) as already described elsewhere (Bel Hadjltaief et al., 2014). The XRD patterns of TiO_2–clay catalyst show the appearance of peaks at 2θ values of 25.281°, 37.934°, 48.376°, 55.296° and 62.728° corresponding to the (101), (103), (200), (105) and (213) planes of anatase type (Ao et al., 2008 Binitha and Sugunan, 2006) matching with (JCPDS No. 21-1272). Other crystal phase corresponding to

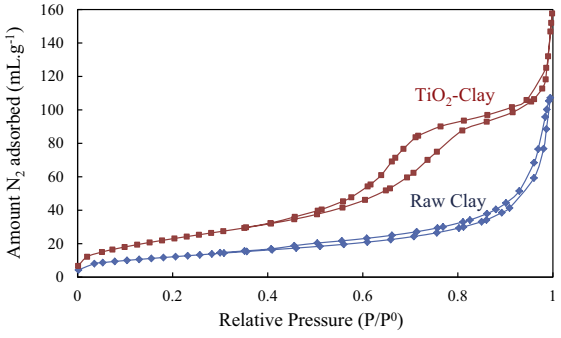

Figure 1 Nitrogen adsorption–desorption isotherms of the raw clay and TiO_2–clay photocatalyst.

Table 1 Texture properties of the different materials.

Texture properties	Samples	
	Raw clay	TiO_2–clay
Surface area, S_{BET} (m^2/g)	36.7	116.7
Total pore volume (cm^3)	0.13	0.26
Pore diameter (nm)	2.24	7.06
Porosity, χ (%)	19	29
Crystallite size, D (nm)	–	16.88
Anatase content, A (%)	–	96.17

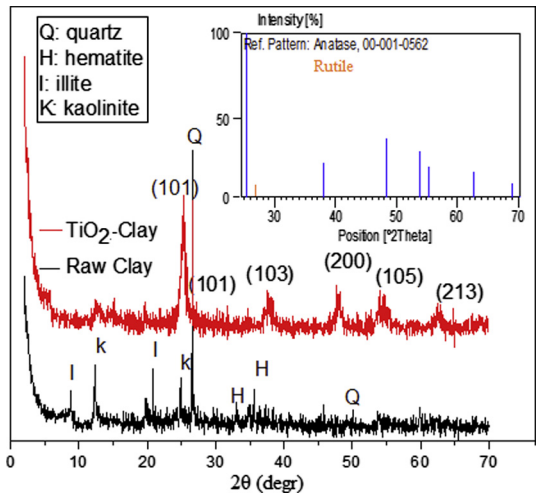

Figure 2 XRD patterns of the raw clay and TiO_2–clay.

peak at and 27.234° were assigned the diffraction peak of (1 0 1) of rutile (JCPDS No. 21-1272) (Lin et al., 2011).

The relative content of anatase and rutile, as listed in Table 1, was estimated using Spurr–Myers equation (Eq. (6)) (Spurr and Myers, 1957):

$$A\ (\%) = \frac{I_A}{I_A + 1.265 \times I_R} \times 100$$

where A (%) is the relative content of anatase, I_A and I_R are the intensities of the anatase (1 0 1) peak at $2\theta = 25.281°$ and the rutile (1 0 1) peak at $2\theta = 27.234°$.

The anatase content of TiO_2–clay was then 96.168. This value shows that the anatase is highly predominant in the sample. The main active crystal phases of TiO_2 are anatase and rutile. According to Ambrus et al. (2008), photocatalyst containing the anatase phase is more efficient than the rutile one. This also suggests that the catalyst (TiO_2–clay) with more than 96% TiO_2 in anatase form will improve the photocatalytic activity (Ambrus et al., 2008).

Based on the XRD results, the average crystal size of TiO_2 was calculated using the Debye–Scherrer equation as follows (Eq. (7)):

$$D = \frac{K\lambda}{\beta Cos(\theta)}$$

where D is the average crystallite size (nm), λ the wavelength of the X-ray radiation ($\lambda = 0.1540$ nm), K the Scherrer constant ($K = 0.9$), β the full-width at half maximum (FWHM) of the (1 0 1) plane and θ is the Bragg angle. The average sizes of TiO_2 crystallite in the catalyst are listed in Table 1.

The infrared spectra of raw clay and TiO_2/clay are shown in Fig. 3 (curves a and b, respectively). The FTIR spectrum of raw clay shows bands at 3630 and 3440 cm^{-1} in the –OH stretching region; these two bands are assigned to the –OH stretching vibration of the structural hydroxyl groups in the clay and the water molecules present in the interlayer, respectively (Mishra and Rao, 2004; Xu et al., 2004; Binitha and Sugunan, 2006; Bineesh et al., 2010). These bands at 3630 and 3440 cm^{-1} broaden due to the introduction of single bond OH groups: this is interpreted as impregnating effect (Binitha and Sugunan, 2006; Kurian and Sugunan, 2003). Moreover, the band at around 1600 cm^{-1} is assigned to the bending

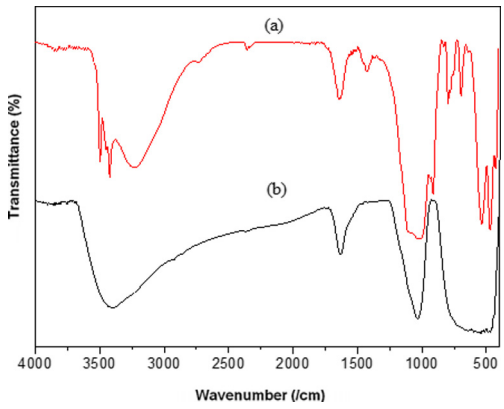

Figure 3 FTIR spectra of the raw clay (a) and TiO_2–clay (b).

vibrations of water, and the one at around 1060 cm^{-1} corresponds to the asymmetric stretching vibrations of SiO_2 in tetrahedric form (Carriazo et al., 2010). The spectrum of the TiO_2–clay (Fig. 1b) exhibits the characteristic transmittance peaks of raw clay (Fig. 3a), the appearance of broad absorption band was observed in the range of 1825–3736 cm^{-1} (Fig. 3b) and was ascribed to the introduction of single bond OH groups of the pillar, described as a impregnation effect in previous studies (Kurian and Sugunan, 2003) dealing with the insertion of TiO_2 in clay.

Coupled diagrams of differential thermal analysis (DTA) and thermogravimetric analysis (TG) of the raw (a) and TiO_2–clay (b) materials are presented in Fig. 4. The raw clay presented a total loss of mass about 14% between 29 °C and 1000 °C. The first mass loss (11%) obtained until 200 °C was due to the removal of the moisture and zeolitic water (Caillère et al., 1982; Brown, 1988). The second mass loss (3%) observed at 420 °C is due to the elimination of constitutional water resulting from the dehydroxylation of the clay minerals (Caillère et al., 1982; Brown, 1988). The third peak of mass loss (2%) occurring at 680 °C corresponds to the decomposition of calcite ($CaCO_3$). In addition to the peak observed for the raw clay, the TiO_2–clay presents intense endothermic peaks located generally in the range of 200–500 °C. From the TGA data of the as-prepared powders, one can presume that TiO_2 is formed.

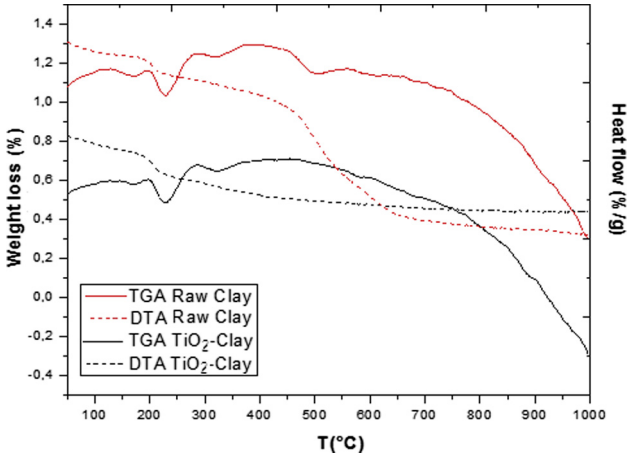

Figure 4 TGA/DTA diagram of the raw clay and TiO_2–clay.

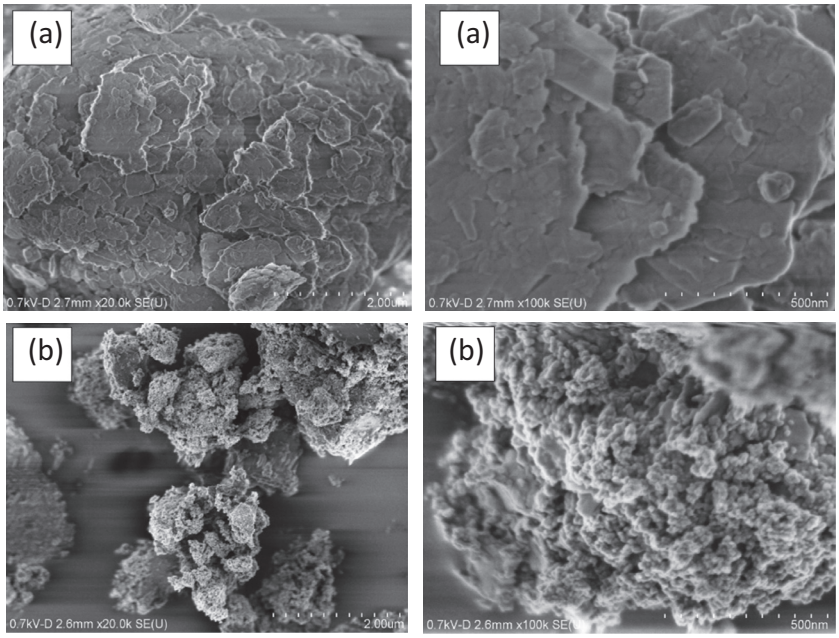

Figure 5 SEM image of (a) the raw clay and (b) TiO_2–clay.

The SEM micrographs of natural clay and TiO_2 clay are presented in Fig. 5 which are quite helpful to clarify the change in the morphological features upon an impregnation process. Clearly, the surface morphology of natural clay (Fig. 5a) is different from that of TiO_2–clay (Fig. 5b). The raw clay presents larger particle aggregates with smooth surfaces whereas after treatment with Ti isopropoxide, uniform TiO_2 grains of about 10–30 nm were observed on the surface clay. Thus we can conclude on a homogeneous distribution of TiO_2 grains on the raw material.

3.2. Photocatalytic degradation of reactive blue 19

Fig. 6 shows that pure photolysis by UV solar and UVA irradiation without a catalyst was unable to degrade RB19. On the contrary, in the presence of the TiO_2–clay catalyst, and in absence of visible light and UVA, a maximal RB19 conversion was found around 20% which becomes stable after 180 min reaction time. This RB19 removal efficiency can be ascribed

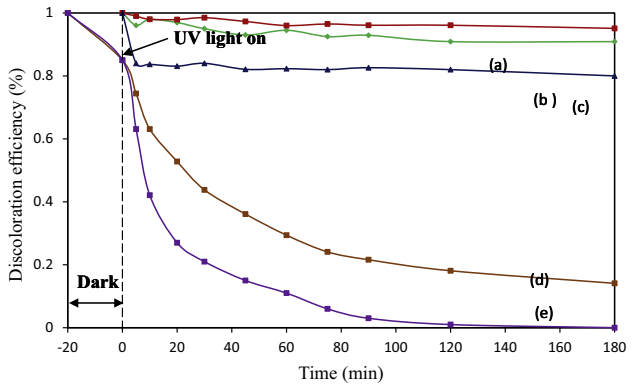

Figure 6 Photocatalytic oxidation of RB19 at various conditions: (a) UV-Solar; (b) UV-A; (c) TiO_2−clay; (d) UV-Solar/TiO_2−clayand (e) UV-A/TiO_2−clay.

to the adsorption of RB19 on the catalytic surface of TiO_2. For the sake of comparison (figure not shown), a non-impregnated clay has been tested and only 5% removal efficiency had been obtained after 180 min of time on stream. The experimental data show that the TiO_2–clay photocatalyst was highly photoactive in RB19 degradation under UV light. After 90 min of irradiation, 99% of RB19 was degraded. The degradation efficiency in the presence of solar light was lower than UV irradiation, since TiO_2–clay photocatalyst is mainly photoactive in UV_A. Same time of irradiation resulted in 78% degradation of RB19 in exposed solar light.

The photocatalytic degradation of RB19 under the two sources of irradiation was described by first order reaction kinetics and the rate constants for TiO_2–clay + solar and TiO_2–clay + UVA were calculated to be 0.009 and 0.016 s^{-1}, respectively. Under adsorption, the reactions would be zeroth order kinetics. The rate constant for TiO_2–clay during the first 30 min was calculated to be 0.071 s^{-1}. Several authors reported that degradation of RB19 by catalysts modified by TiO_2 under visible light or UVB also followed first order kinetics. Thus, for example, Zhang et al., 2011 reported that degradation of RB19 by TiO_2-FAU-type zeolites under visible light also followed first order kinetics with a rate constant of 0,00,015 s^{-1}.

3.3. Photochemical oxidation

3.3.1. Effect of oxidating agents

From the results presented above, TiO_2–clay has a better photocatalytic activity in UVA than UV solar. Thus, TiO_2–clay was further investigated for degradation of RB19 under UVA in photochemical reaction with different oxidating agents. The effect of these agents on the efficiency of RB19 degradation is presented in Fig. 7. The chosen agents such as hydrogen peroxide (H_2O_2), potassium peroxodisulfate ($K_2S_2O_8$) and sodium carbonate (Na_2CO_3) behaved differently in the photochemical degradation of RB 19. The results show that the degradation was most effective with the photolysis of

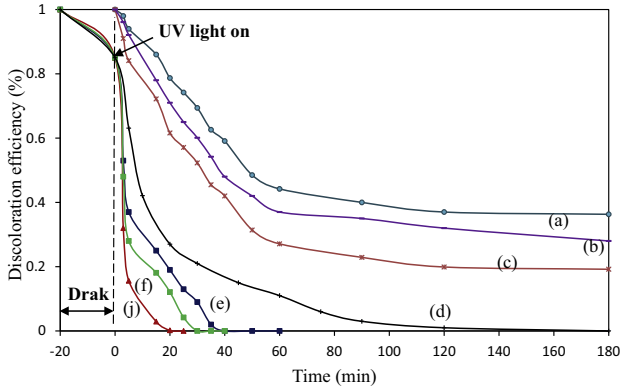

Figure 7 Photochemical oxidation of RB19 at various conditions: (a) UV_A/Na_2CO_3; (b) $UV_A/K_2S_2O_8$; (c) UV_A/H_2O_2; (d) UV_A/TiO_2–clay; (e) TiO_2–clay + Na_2CO_3/UV_A; (f) TiO_2–clay + $K_2S_2O_8/UV_A$ and (j) TiO_2–clay + H_2O_2/UV_A.

H_2O_2, followed by the photolysis of $K_2S_2O_8$ and photolysis of Na_2CO_3 systems (Fig. 7). These later results can be attributed to the formation of both $HO^{\cdot}$ and $SO_4^{\cdot-}$ radicals during the reaction leading to a higher conversion. The UV/Na_2CO_3 system also had the lowest RB 19 degradation rate constant, because $CO_3^{\cdot-}/HCO_3^{\cdot}$ has a lower radical reaction rate constant, and oxidizing power (E° = 1.78 V) in comparison with the oxidizing power of $HO^{\cdot}$ (E° = 2.80 V) and $SO_4^{\cdot-}$(E° = 2.05 V).

Various studies have noted that $K_2S_2O_8$ and H_2O_2 can be decomposed by direct UV radiation (Manuel et al., 2013; Muruganandham and Swaminathan, 2006; Saien et al., 2011). However, no data are available on the generation of $HCO_3^{\cdot}$ and $CO_3^{\cdot-}$ radicals by direct UV radiation in the presence of CO_3^{2-} or HCO_3^{-}. Thus, the generation of $CO_3^{\cdot}$– radicals in aqueous solution, including one-electron oxidation of bicarbonate or carbonate by hydroxyl radical (Canonica et al., 2005).

The generation of oxidizing agents, such as $HO^{\cdot}$, $S_2O_8^{2-\cdot}$, $HCO_3^{\cdot}$ and $CO_3^{\cdot-}$ is given by the following chain reaction (Eqs. (3)–(6)) (Manuel et al. 2013; Muruganandham and Swaminathan, 2006; Saien et al., 2011a,b; Kumar and Mathur 2006).

$$H_2O_2 + h\nu \rightarrow 2HO^{\cdot} \quad (3)$$

$$S_2O_8^{2-} + h\nu \rightarrow 2S_2O_4^{\cdot-} \quad (4)$$

$$HO^{\cdot} + CO_3^{2-} \rightarrow HCO_3^{\cdot-} + OH^{-} \quad (5)$$

$$HO^{\cdot} + HCO_3^{-} \rightarrow CO_3^{\cdot-} + H_2O \quad (6)$$

Fig. 7 also shows the degradation is more efficient when reaction is performed in the presence of the TiO_2–clay catalyst, upon H_2O_2, $K_2S_2O_8$, and Na_2CO_3 addition and UV irradiation, the reduction for 20 min of treatment was 99.8% with the H_2O_2 + TiO_2–clay/UV, 87.9% with $K_2S_2O_8$ + TiO_2–clay/UV, and 80.1% with Na_2CO_3 + TiO_2–clay/UV. However, addition of the H_2O_2, $K_2S_2O_8$, and Na_2CO_3 agents to photocatalytic process showed an impressive performance for RB19 decolorization. Thus, the combination of photocatalyst and oxidizing agent is found to be the most efficient for the decolorizing RB19 under high UV photon flux (Muruganandham and Swaminathan, 2006).

On the other hand, the high photodegradation of RB 19 by TiO_2–clay is due to the anatase phase stability of the used photocatalyst. The anatase nanocrystals generate various oxidizing species by UV irradiation, which simultaneously attack the pre-enriched RB19 dye from many different directions. As a result, the RB 19 dye is in no time cleaved into small molecule intermediates. Subsequently, the resultants diffuse out of the pores into the solution. In this process, the hydroxyl radical, the sulfate and carbonate radicals are efficiently used because of the synchronous role of adsorption and photocatalytic oxidation, generating the excellent activity (Muruganandham and Swaminathan, 2006; Manuel et al., 2013).

The possible reaction scheme for the photocatalytic degradation of RB 19 from aqueous solution is given in Eqs. (6)–(12).

(i) photo-excitation with light of an energy greater than the TiO_2 band gap, which promotes the transfer of an electron, e^-, from the valence band to the conduction band, leaves an electronic vacancy or hole, h^+, in the valence band, and thus generates an electron–hole pair (Eq. (6)):

$$\text{Clay} \approx TiO_2 + h\nu(\text{UV}) \rightarrow \text{clay} \approx TiO_2(h^+) + \textit{clay} \approx TiO_2(e^-) \quad (6)$$

(ii) Generation of hydroxyl, $OH^{\cdot}$,$CO_3^{\cdot}$ $SO_4^{\cdot-}$,radicals: (Eq. (6)).

$$h^+ + H_2O \rightarrow HO^{\cdot} + H^+ \quad (7)$$

$$\text{Clay} \approx TiO_2(h^+) + CO_3^{2-} \rightarrow CO_3^{\cdot-} + OH^- \quad (8)$$

$$\text{clay} \approx TiO_2(h^-) + H_2O_2 \rightarrow \text{Clay} \approx TiO_2 + HO^{\cdot} + OH^- \quad (9)$$

$$\text{clay} \approx TiO_2(h^-) + S_2O_8^{2-} \rightarrow \text{Clay} \approx TiO_2 + S_2O_4^{\cdot-} + S_2O_4^{2-} \quad (10)$$

(iii) Attack of hydroxyl and sulfate radicals to adsorbed dye and their mineralization to CO_2 and H_2O:

$$\text{clay} \approx TiO_2 + \text{RB19} + \text{Oxidizing species} \rightarrow \text{Reactions intermediates} \quad (11)$$

$$\text{Reactions intermediates} + \text{Oxidizing species} \rightarrow CO_2 + H_2O \quad (12)$$

3.3.2. *Effect of dye concentration and subsequent kinetic study*

Fig. 8 shows the kinetics of the photocatalytic degradation of RB 19 solution using different initial concentrations. It is evident that the photodegradation rate depends on the initial concentration of this organic pollutant. At 20 min of irradiation time, the increase of dye concentration from 75 to 200 mg/L leads to a decrease of the degradation from 99.6% to 39.8%.

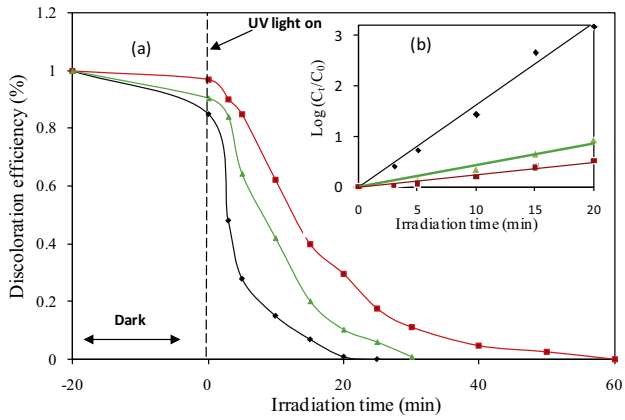

Figure 8 Effect of the initial dye concentration on the discoloration efficiency of RB 19: (■) 75 mg/L; (▲) 150 mg/L and (♦) 200 mg/L. (a) Discoloration efficiency versus irradiation time. (b) Rate constants as a function of the initial dye concentration.

The rate of degradation is related to the OH radical formation on catalyst surface and probability of OH radical reacting with dye molecule. For all initial dye concentrations, the catalyst weight and light intensity are the same. Since the generation of hydroxyl radical remains constant, the probability of dye molecule to react with hydroxyl radical decreases. At high initial dye concentration, the path length of photon entering into the solution also decreases. Thus, the photocatalytic degradation efficiency decreases, but at low concentration the reverse effect is observed thereby increasing photon absorption by the catalyst (Krishnakumar et al., 2010). The large amount of adsorbed dye may also have a competing effect on the adsorption of oxygen and OH onto the surface of catalyst.

Generally, first-order kinetics is appropriate for photocatalytic reactions (Bel Hadjltaief et al., 2013). The formation of reactive intermediate products of RB 19 and their reaction with hydroxyl radicals could explain the change of the degradation rates.

Kinetics model as follows:

$$-r_A = -\frac{dC}{dt} = kt \tag{13}$$

After integration of Eq. (6), the following equation is obtained:

$$\ln\left(\frac{C_0}{C}\right) = kt \tag{14}$$

where r_A is the oxidation rate of the RB 19 (mg (min^{-1})), k the apparent constant of the reaction rate (the constant of first order reaction), C the concentration of the RB 19 (mg), C_0 the initial concentration of RB 19, t the time required for the initial concentration of RB 19, C_0 to become C(min).

The plot of $\ln\left(\frac{C_0}{C}\right)$ versus t with different initial concentrations of RB 19 is shown in the insert in Fig. 8. All the curves showed a good linear correlation ($R^2 > 0.99$), suggesting that the degradation of RB 19 by H_2O_2 + TiO_2–clay/UV followed a first-order kinetic. Under the same experimental conditions, the kinetic constant of RB 19 decolorization was 0.162, 0.042 and 0.024 min^{-1}, while the initial concentration was 75, 150 and 200 mg/L, respectively.

Experimental results showed that the destruction rates of RB 19 decolorization by H_2O_2 + TiO_2–clay/UV fitted the Langmuir–Hinshelwood (L–H) kinetic model as follows:

$$-\frac{dC}{dt} = \frac{K_r K_e C}{1 + K_e C} \tag{15}$$

where K_r is the reaction rate constant (mg/L min) and K_e is the adsorption coefficient of the MTBE (l/mg). With regard to Eq. (9), the constant k can be defined as follows:

$$\frac{1}{k} = \frac{1}{K_e K_r} + \frac{C_0}{K_e} \tag{16}$$

K_r was calculated from the slope of the $1/k$ versus C_0 plot, and K_e was then calculated from intercept of this plot (Fig. 9). The reaction constant and the adsorption coefficient of the reactant as well as correlation coefficient (R^2) values for RB 19 degradation at different initial RB 19 concentrations are presented in Table 2.

3.4. Mineralization of RB19 photochemical process

The mineralization/degradation of the process was monitored by UV–Vis absorption spectra to investigate the structural change of R19, HPLC and DCO. Degradation experiments were performed at pH 5.51, 75 mg/L dye concentration, 100 mg of the TiO_2–clay catalyst, and 250 mg/L of H_2O_2.

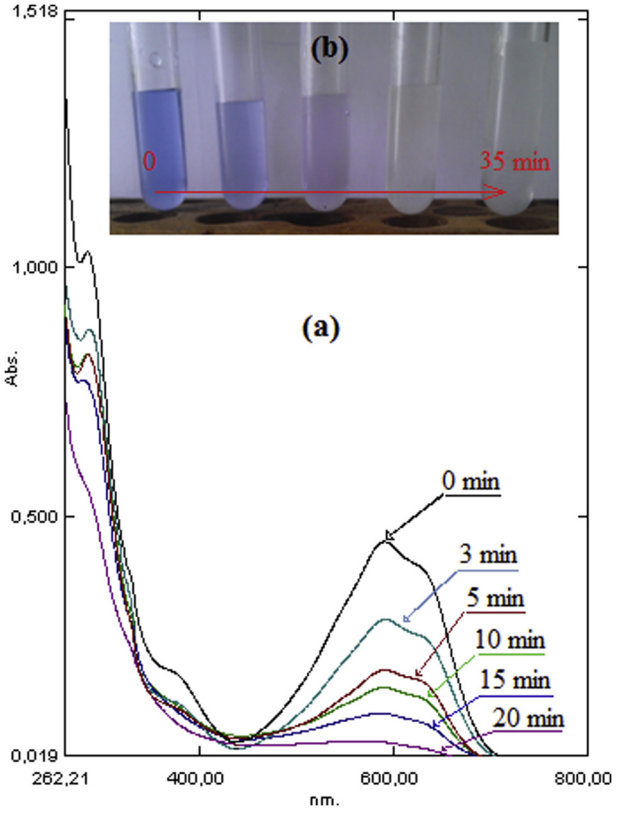

Figure 9 Evolution of UV–Visible spectra of RB19.

Table 2 The values of reaction constant and the adsorption coefficient of the reactant.

Catalyst	K_r (mg(min^{-1}))	K_e (mg^{-1})	R^2
TiO_2–clay	0.2835	0.0621	0.990

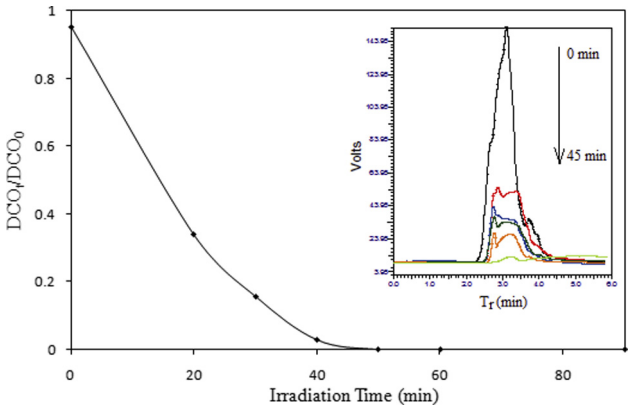

Figure 10 Evaluation of COD and HPLC chromatograms with treatment time.

Solution samples were analyzed in time intervals 0–35 min. Thus, one can note that the corresponding degradation efficiency curve in terms of percent efficiency (%) is the filled-square symbol plots in Fig. 9.

Based on the analysis of UV–Vis presented in Fig. 9a, the dye reached the peak of maximum absorption at three wavelengths (λ) namely: 227, 325, and 592 nm (Guimarães et al., 2012; Siddique et al., 2011). The peak observed in the visible region at 592 nm was due to the blue color of the chromophore (Guimarães et al., 2012; Siddique et al., 2011). This figure shows a high decrease of RB19 absorption at the wavelength of 591 nm observed during the first few 20 min. Fig. 9b reports a picture of color change in the reaction solution during the degradation of RB 19 which indicated some highly colored intermediate compounds. Moreover, these colored intermediates are more refractory and difficult to oxidize (Violet and yellow color). After treatment (30 min of reaction), the solution becomes colorless, this result shows the full discoloration of RB 19 in the solution.

A COD removal efficiency was calculated and plotted as a function of the irradiation time (Fig. 10). As expected COD decreases, and therefore the COD removal efficiency increases, with irradiation time. After 45 min of reaction, the maximal reaction time, the COD removal efficiency reached 98%. In the same condition and the same processing time, the RB 19 peak with the RT of 3.112 completely disappears from the HPLC chromatogram (Fig. 10b), which indicates that TiO_2–clay exhibits excellent photocatalytic activity in the degradation of RB 19.

4. Conclusions

A TiO_2-coated Tunisian clay was synthesized by a typical impregnation method. The physical characterization of these catalysts clearly shows that titania was incorporated homogeneously on the surface of the catalyst. Then, the photocatalytic/photochemical oxidation of anionic reactive blue 19 (RB 19) was tested on such heterogeneous materials. In addition, the effect of UVA and solar irradiation was also studied. TiO_2–clay demonstrated an effective degradation of RB 19 over UVA and solar irradiation. Moreover, the high photodegradation of RB 19 by TiO_2–clay is due to the anatase phase stability of the used photocatalyst (Omri et al., 2014).

Moreover, in this study, the effects of various oxidants such as hydrogen peroxide (H_2O_2), potassium peroxodisulfate ($K_2S_2O_8$) and sodium carbonate (Na_2CO_3) on RB 19 degradation were investigated. It was shown that H_2O_2 was a promising oxidant for promoting RB 19 degradation under UV_A.

A kinetic study was performed and showed that the discoloration of dyes followed a pseudo-first-order rate law. 100% discoloration was achieved after 20 min of UV–Vis irradiation of the aqueous solution. However, UV–Vis, HPLC and chemical oxygen demand measurements indicated, that a longer reaction time (of around 45 min) was required for achieving the dye mineralization.

Finally this study clearly demonstrated the applicability of TiO_2–clay for catalytic treatment of RB 19. Even though no traces of metal were found in the solutions, runs are in course in order to check the reusability of the catalyst, in using 5 cycle runs for the dye elimination.

References

Ambrus, Z., Mogyorósi, K., Szalai, A., Alapi, T., Demeter, K., Dombi, A., Sipos, 2008. Low temperature synthesis, characterization and substrate-dependent photocatalytic activity of nanocrystalline TiO_2 with tailor-made rutile to anatase ratio. Appl. Catal. A: Gen. 340, 153–161.

Ao, Y., Xu, F.J.D., Shen, X., Yuan, C., 2008. Low temperature preparation of anatase TiO_2-coated activated carbon. Colloids Surf., A 312 (2–3), 125–130.

Bel Hadjltaief, H., Costa, Da., Gálvez, M.E., Benzina, M., 2013. Influence of operational parameters in the heterogeneous photo-fenton discoloration of wastewaters in the presence of an iron-pillared clay. Ind. Eng. Chem. Res. 52, 16656–16665.

Bel Hadjltaief, H., Da Costa, P., Beaunier, P., Gálvez, M.E., Benzina, M., 2014. Fe–clay-plate as a heterogeneous catalyst in photo-Fenton oxidation of phenol as probe molecule for water treatment. Appl. Clay Sci. 91–92, 46–54.

Bineesh, K.V., Kim, D.K., Cho, H.J., Park, D.W., 2010. Synthesis of metal-oxide pillared montmorillonite clay for the selective catalytic oxidation of H_2S. J. Ind. Eng. Chem. 16, 593–597.

Binitha, N.N., Sugunan, S., 2006. Preparation, characterization and catalytic activity of titania pillared montmorillonite clays. Microporous Mesoporous Mater. 93, 82–89.

Brown, M.E., 1988. Introduction to Thermal Analysis, Techniques and Applications. Chapman and Hall, London, 211.

Caillère, S., Henin, S., Rautureau, M., 1982. Minéralogie des argiles, 2nd ed. Masson, Paris.

Canonica, S., Kohn, T., Mac, M., Real, F.J., Wirz, J., Von, G.U., 2005. Photosensitizer method to determine rate constants for the reaction of carbonate radical with organic compounds. Environ. Sci. Technol. 39, 9182–9188.

Carneiro, A.P., Nogueira, R.F.P., Zanoni, M.V.B., 2007. Homogeneous photodegradation of C.I. reactive blue 4 using a photo-Fenton process under artificial and solar irradiation. Dyes Pigm. 74, 127–132.

Carriazo, J.G., Moreno-Forero, M., Molina, R.A., Moreno, S., 2010. Incorporation of titanium and titanium-iron species inside a smectite-type mineral for photocatalysis. Appl. Clay Sci. 50, 401–408.

Chen, D., Zhu, H., Wang, X., 2014. A facile method to synthesize the photocatalytic TiO_2/montmorillonite nanocomposites with enhanced photoactivity. Appl. Surf. Sci.. http://dx.doi.org/10.1016/j.apsusc.2014.05.085.

Dammak, N., Fakhfakha, N., Fourmentin, S., Benzina, M., 2013. Natural clay as raw and modified material for efficient o-xylene abatement. J. Environ. Chem. Eng. 1, 667–675.

De Souza, K.V., Peralta-Zamora, P., Zawadzki, S.F., 2008. Immobilization of iron(II) in alginate matrix and its use in textile dye degradation by Fenton. Quim. Nova 31, 1145–1149.

Djellabi, R., Ghorab, M.F., Cerrato, G., Morandi, S., Gatto, S., Oldani, V., Michele, A.Di., Bianchi, C.L., 2014. Photoactive TiO_2-montmorillonite composite for degradation of organic dyes in water. J. Photochem. Photobiol. A: Chem.. http://dx.doi.org/10.1016/j.jphotochem.2014.08.017.

Dvininova, E., Popovici, E., Pode, R., Cocheci, L., Barvinschi, P., Nica, V., 2009. Synthesis and characterization of TiO_2-pillared Romanian clay and their application for azoic dyes photodegradation. J. Hazard. Mater. 167, 1050–1056.

Eloussaief, M., Mourad, B., 2010. Efficiency of natural and acid-activated clays in the removal of Pb(II) from aqueous solutions. J. Hazard. Mater. 178, 753–757.

Emna, Hmani, Elaoud, Sourour Chaabane, Samet, Youssef, Abdelhédi, Ridha, 2009. Electrochemical degradation of waters containing O-toluidine on PbO_2 and BDD anodes. J. Hazard. Mater. 170, 928–933.

Garrido-Ramírez, E.G., Theng, B.K.G., Mora, M.L., 2010. Clays and oxide minerals as catalysts and nanocatalysts in Fenton-like reactions—a review. Appl. Clay Sci. 47, 182–192.

Gok, O.A., Ozcan, S., Adnan, O., 2010. Adsorption behavior of a textile dye of reactive blue 19 from aqueous solutions onto modified bentonite. Appl. Surf. Sci. 256, 5439–5443.

Guimarães, J.R., Maniero, M.G., Nogueirade Araújo, R., 2012. A comparative study on the degradation of RB-19 dye in an aqueous medium by advanced oxidation processes. J. Environ. Manage. 110, 33–39.

Hamza, W., Chtara, C., Benzina, M., 2013. Retention of organic matter contained in industrial phosphoric acid solution by raw tunisian clays: kinetic equilibrium study. J. Chem. 2013, 9–17.

He, Z., Lin, L., Song, S., Xia, M., Xu, L., Ying, H., Chen, J., 2008. Mineralization of C.I. reactive blue 19 by ozonation combined with sonolysis: performance optimization and degradation mechanism. Sep. Purif. Technol. 62, 376–381.

Herney-Ramirez, J., Vicente, M.A., Madeira, L.M., 2010. Heterogeneous photo-Fenton oxidation with pillared clay based catalysts for wastewater treatment: a review. Appl. Catal. B 98, 10–26.

Jiang, X., Cai, K., Zhang, J., Shen, Y., Wang, S., Tian, X., 2011. Synthesis of a novel water-soluble chitosan derivative for flocculated decolorization. J. Hazard. Mater. 185, 1482–1488.

Koyuncu, I., 2002. Reactive dye removal in dye/salt mixtures by nanofiltration membranes containing vinylsulphone dyes: effects of feed concentration and cross flow velocity. Desalination 143, 243–253.

Krishnakumar, B., Selvam, K., Velmurugan, R., Swaminathan, M., 2010. Influence of operational parameters on photomineralization of Acid Black 1 with ZnO. Desalin. Water Treat. 24, 132–139.

Kumar, A., Mathur, N., 2006. Photocatalytic degradation of aniline at the interface of TiO2 suspensions containing carbonate ions. J. Colloid Interface Sci. 300, 244–252.

Kurian, M., Sugunan, S., 2003. Liquid phase benzylation of o-xylene over pillared clays. Ind. J. Chem. A. 42, 2480–2486.

Lin, S.H., Chiou, C.H., Chang, C.K., Juang, R.S., 2011. Photocatalytic degradation of phenol on different phases of TiO_2 particles in aqueous suspensions under UV irradiation. J. Environ. Manage. 92, 3098–3104.

Manuel, S.P., Mahmoud, M.A., Raúl, O.P., José, R.U., Antonio, J.M., 2013. Comparative study of the photodegradation of bisphenol A by $HO^{\bullet}$, $SO4^{\bullet-}$ and $CO3^{\bullet-}/HCO3^{\bullet}$ radicals in aqueous phase. Sci. Total Environ. 463–464, 423–431.

McCallum, J.E.B., Madison, S.A., Alkan, S., Depinto, R.L., Wahl, R.U.R., 2000. Analytical studies on the oxidative degradation of the reactive textile dye Uniblue A. Environ. Sci. Technol. 34, 5157–5164.

Mishra, B.G., Rao, G.G., 2004. Physicochemical and catalytic properties of Zr-pillared montmorillonite with varying pillar density. Microporous Mesoporous Mater. 70, 43–50.

Moussavi, G., Mahmoudi, M., 2009. Removal of azo and anthraquinone reactive dyes from industrial wastewaters using MgO nanoparticles. J. Hazard. Mater. 168, 806–812.

Muruganandham, M., Swaminathan, M., 2006. TiO_2–UV photocatalytic oxidation of Reactive Yellow 14: Effect of operational parameters. J. Hazard. Mater. B. 135, 78–86.

Omri, A., Benzina, M., Bennour, F., 2014. Industrial application of photocatalysts prepared by hydrothermal and sol–gel methods. J. Ind. Eng. Chem.. http://dx.doi.org/10.1016/j.jiec.2014.02.045, in press.

Pirkarami, A., Olya, M.E., Tabibian, S., 2013. Treatment of colored and real industrial effluents through electrocoagulation using solar energy. J. Environ. Sci. Health A: Toxic/Hazard. Subst. Environ. Eng. 48, 1243–1252.

Qu, J.G., Li, N.N., Liu, B.J., He, J.X., 2013. Preparation of BiVO4/bentonite catalysts and their photocatalytic properties under simulated solar irradiation. Mater. Sci. Semicond. Process. 16, 99–105.

Saien, J., Ojaghloo, Z., Soleymani, A.R., Rasoulifard, M.H., 2011a. Homogeneous and heterogeneous AOPs for rapid degradation of Triton X-100 in aqueous media via UV light, nano titania hydrogen peroxide and potassium persulfate. Chem. Eng. J. 167, 172–182.

Saien, J., Soleymani, A.R., Sun, J.H., 2011b. Parametric optimization of individual and hybridized AOPs of $Fe^{2+}/H_2O_2$and $UV/S_2O_8^{2-}$ for rapid dye destruction in aqueous media. Desalination 279, 298–305.

Siddique, M., Farooq, R., Khan, Z.M., Khan, Z., Shaukat, S.F., 2011. Enhanced decomposition of reactive blue 19 dye in ultrasound assisted electrochemical reactor. Ultrason. Sonochem. 18, 190–196.

Sing, K.S.W., Williams, R.T., 2004. The use of molecular probes for the characterization of nanoporous adsorbents. Particle Particle Syst. Charact. 21, 71–79.

Sing, K.S.W., Everett, D.H., Haul, R.A.W., Moscou, L., Pierotti, R.A., Rouquerol, N., Siemieniewska, T., 1985. Reporting physisorption data for gas/solid systems. Pure Appl. Chem. 57, 603–619.

Song, S., Yao, J., He, Z., Qiu, J., Chen, J., 2008. Effect of operational parameters on the decolorization of C.I. reactive blue 19 in aqueous solution by ozone-enhanced electrocoagulation. J. Hazard. Mater. 152, 204–210.

Spurr, R.A., Myers, H., 1957. Quantitative analysis of anatase rutile mixtures with an X-ray diffractometer. Anal. Chem. 29, 760–762.

Wang, H., Li, Q., He, N., Wang, Y., Sun, D., Shao, W., Yang, K., Lu, Y., 2009. Removal of anthraquinone reactive dye from wastewater by batch hydrolytic–aerobic recycling process. Sep. Purif. Technol. 67, 180–186.

Xu, X., Pan, Y., Cui, X., Sou, Z., 2004. Catalytic combustion of methane over Ti-pillared clay supported copper catalysts. J. Nat. Gas Chem. 13, 204–208.

Zhang, G., Choi, W., Kim, S.H., Hong, S.B., 2011. Selective photocatalytic degradation of aquatic pollutants by titania encapsulated into FAU-type zeolites. J. Hazard. Mat. 188, 198–205.